

Correlating Phase Behaviour with Photophysical Properties in Mixed-Cation Mixed-Halide Perovskite Thin Films

*Claire Greenland, Adam Shnier, Sai K. Rajendran, Joel A. Smith, Onkar S. Game, Daniel Wamwangi, Graham A. Turnbull, Ifor D. W. Samuel, David G. Billing and David G. Lidzey**

C. Greenland, J. A. Smith, Dr O. S. Game, Prof. D. G. Lidzey
Department of Physics and Astronomy
University of Sheffield
Hicks Building, Hounsfield Road
Sheffield S3 7RH, United Kingdom
E-mail: d.g.lidzey@sheffield.ac.uk

A. Shnier, Prof. D. G. Billing
School of Chemistry
University of the Witwatersrand
Johannesburg 2050, South Africa

Dr. S. K. Rajendran, Prof. G. A. Turnbull, Prof. I. D. W. Samuel
Organic Semiconductor Centre, SUPA
School of Physics and Astronomy
University of St Andrews
North Haugh, St Andrews KY16 9SS, United Kingdom

Prof. D. Wamwangi
School of Physics
University of the Witwatersrand
Johannesburg 2050, South Africa

Keywords: hybrid perovskite solar cells, crystal structure, photoluminescence, charge recombination

Abstract

Mixed cation perovskites currently achieve very promising efficiency and operational stability when used as the active semiconductor in thin-film photovoltaic devices. However an in-depth understanding of the structural and photophysical properties that drive this enhanced performance is still lacking. Here we explore the prototypical mixed-cation mixed-halide perovskite $(\text{FAPbI}_3)_{0.85}(\text{MAPbBr}_3)_{0.15}$, and present temperature-

dependent X-ray diffraction measurements that we correlate with steady state and time-resolved photoluminescence data. Our measurements indicate that this material adopts a pseudo-cubic perovskite α phase at room temperature, with a transition to a pseudo-tetragonal β phase occurring at ~ 260 K. We find that the temperature dependence of the radiative recombination rates correlates with temperature-dependent changes in the structural configuration, and observed phase transitions also mark changes in the gradient of the optical band gap. Our work illustrates that temperature-dependent changes in the perovskite crystal structure alter the charge carrier recombination processes and photoluminescence properties within such hybrid organic-inorganic materials. Our findings have significant implications for photovoltaic performance at different operating temperatures, as well as providing new insight on the effect of alloying cations and halides on the phase behaviour of hybrid perovskite materials.

1 Introduction

Recent years have seen rapid progress in the development of high efficiency perovskite solar cells, with new material systems, compositional engineering and passivation techniques used to increase power conversion efficiencies beyond 24%.^[1] Indeed, perovskite materials have many favourable properties for photovoltaic applications, such as strong optical absorption,^[2] long diffusion lengths,^[3] long carrier lifetimes^[4] and high defect tolerance.^[5] They can also be deposited from solution using low cost, low temperature processes, with large area devices being fabricated by methods such as slot-die coating and spray coating.^[6;7]

A perovskite material is defined as any material adopting the structure ABX_3 , where A is a monovalent cation (typically Cs or alkylammonium ions), B is a divalent metal cation (commonly Pb or Sn) and X is a halide anion (commonly I, Br or Cl). The single-cation hybrid perovskite $MAPbI_3$, where MA is the organic molecule methylammonium ($CH_3NH_3^+$), has been utilised as an absorber layer for perovskite solar cells (PSCs) since their advent in 2009.^[8] Whilst $MAPbI_3$ has dominated the PSC research field for a number of years, its poor thermal stability and sub-optimal band gap limit its usefulness for photovoltaic applications.^[9;10]

The replacement of MA with the larger cation $HC(NH_2)_2^+$ (formamidinium or FA) to form $FAPbI_3$ has been shown to reduce the band gap, bringing it closer to the Shockley-Queisser optimum band gap for solar cell absorber layers (~ 1.4 eV).^[11] Although at room temperature $FAPbI_3$ does not form a stable cubic perovskite phase, it is possible to stabilise the cubic perovskite phase by incorporating

20% MA back into the A-site.^[12] Additionally the inclusion of a mixed halide into the perovskite allows the band gap to be further tuned and its stability and optoelectronic properties to be optimised.^[13] As such, highly efficient perovskite solar cell (PSC) devices have been demonstrated based on the mixed cation lead mixed halide perovskite system $(\text{FAPbI}_3)_{1-x}(\text{MAPbBr}_3)_x$ ($0 < x < 1$), in which $x = 0.15$ has been shown to yield optimum device performance.^[14;15;16] Despite advances in device performance arising on the basis of empirical studies, the fundamental properties of these multi-cation materials are not yet fully understood.

A number of research groups have used temperature-dependent techniques to gain a deeper understanding of hybrid perovskite materials and their optoelectronic properties. Such studies provide insight into the intrinsic properties of the material and have relevance to the practical operation of PSC devices, which can typically be exposed to a wide range of temperatures during operation.^[17] The phase behaviour of mixed cation, mixed halide perovskites has been investigated by a number of authors. Measurements made by Xie *et al.* revealed that materials in the $(\text{FAPbI}_3)_{1-x}(\text{MAPbBr}_3)_x$ compositional range generally adopt a cubic perovskite structure at room temperature, contributing to their superior thermal stability.^[18] Weber *et al.* have also reported a tetragonal-to-cubic phase transition at ~ 280 K for the single halide perovskite $(\text{FAPbI}_3)_{0.8}(\text{MAPbI}_3)_{0.2}$.^[19] However the addition of the mixed halide in $(\text{FAPbI}_3)_{1-x}(\text{MAPbBr}_3)_x$ will have an as yet undocumented and potentially significant effect on the phase behaviour.^[20] Various studies have documented the temperature-dependent charge carrier dynamics and photoluminescence properties of hybrid perovskite materials, and the relationship between phase behaviour and these properties has been studied extensively in MAPbI_3 , most notably by the Herz group.^[21;22] However, this relationship has not yet been explored in mixed-cation mixed-halide systems, despite their superior photovoltaic performance.

In this work, we explore both the optical and structural properties of thin films of the mixed cation, mixed halide perovskite $(\text{FAPbI}_3)_{0.85}(\text{MAPbBr}_3)_{0.15}$ as a function of temperature between 4 K and 350 K. We perform variable temperature powder X-ray diffraction studies over the temperature range 80-350 K in order to identify structural phase transitions. We then compare our findings with results obtained from steady-state photoluminescence and absorption spectroscopy, at a range of temperatures from 4 K to 300 K. We also draw a comparison with time-resolved photoluminescence measurements taken with a streak camera at temperatures from 77 K to 300 K, which allows us to characterise charge carrier recombination dynamics. This combinatorial study of crystal structure with PL and absorption measurements highlights the complex phase behaviour and photophysics at play in alloyed perovskite materials and the implications this has for device performance.

2 Results and Discussion

2.1 Powder X-ray Diffraction

First we discuss variable temperature powder X-ray diffraction (PXRD) data recorded from $(\text{FAPbI}_3)_{0.85}(\text{MAPbBr}_3)_{0.15}$. The perovskite was synthesised and prepared as described in the ‘Experimental Methods’ section, and all spectroscopic measurements in Section 2.2 and 2.3 were made on such polycrystalline films. An SEM image of a typical thin film is shown in Figure S1 in the Supporting Information. To collect PXRD data, a powder was created by scraping thin films from substrates using a razor blade. PXRD data was then recorded at regular temperature intervals while cooling the powder from 315 K to 80 K, and subsequently while re-heating it from 80 K to 350 K.

We plot XRD patterns recorded on cooling and heating cycles in Figure 1A and Figure 1B, respectively. We can immediately identify strong scattering peaks at $Q = 0.997$ and 1.996 \AA^{-1} , which we associate with the (100) and (200) crystal planes of the cubic phase, respectively. We also observe weaker scattering features at 1.412 and 1.728 \AA^{-1} , which correspond to the (110) and (111) crystal planes of the cubic phase, respectively. Careful inspection of Figure 1A and Figure 1B also reveals that there is a gradual shift of all peaks to larger Q at low temperature; this result is consistent with a thermally-induced contraction of the lattice, as we discuss below. It is apparent that as the temperature is reduced to ~ 260 K a series of additional peaks appear at 1.583 , 1.879 and 2.560 \AA^{-1} . The emergence of these peaks can be seen more clearly in Figure S2 (Supporting Information), which displays the full PXRD patterns at all temperatures on both cooling and heating.

For completeness we show the normalised peak positions and peak widths (full width at half-maximum) as a function of temperature in Figure S3 (Supporting Information), which were fitted using a Pearson VII empirical profile. The peaks shift to smaller Q -values as the temperature is increased, with a broadening in the distribution of peak positions observed above 270 K. We also find that as the temperature is reduced between 270 K and 210 K many of the peaks broaden. We attribute much of this broadening to different crystallographic planes no longer being equivalent as the symmetry of the unit cell changes on cooling. For example, the (100) plane becomes inequivalent to (001), resulting in a splitting of peaks. Interestingly, we observe upon heating that the temperature range over which this behaviour is observed shifts to 230-270 K.

To obtain structural information from our scattering data, we have used Rietveld refinements, with details of the modelling given in the ‘Experimental Methods’ section. Figure 1C-E plots the measured and simulated XRD patterns for 80 K, 240 K and 315 K together with the residuals. The

refined models fit well to the experimental data, and this analysis has allowed us to identify a series of different structural changes that occur across the studied temperature range. Specifically, above 260 K we propose that the material assumes a pseudo-cubic α phase approximating the space group $Pm-3m$, as previously reported for single-cation perovskites.^[23;24] This phase is denoted by α in accordance with previous studies referring to a photoactive cubic phase for hybrid perovskites.^[25;19] Over the temperature range 250-90 K, the material appears to adopt a pseudo-tetragonal phase resembling space group $P4/mbm$. This intermediate tetragonal phase has been observed in a study on FAPbI₃ by Weber *et al.*; here we refer to it as the β phase, using the notation convention of Weber and colleagues.^[26] As the temperature is reduced below 90 K, the material assumes a structure which we suggest is a variation on the β phase. This phase (as seen in FAPbI₃ where it appears below ~ 140 K) has also been identified as $P4/mbm$ and is denoted as the γ phase.^[27;28] For each proposed phase, we have included a schematic of the modelled unit cell in Figure 2C-E.

Our identification of these phase transitions is largely based on the temperature dependence of two key parameters: the tilt angle of the lead-halide-lead bond and the lattice parameter ratio $c\sqrt{2}/a$.

In Figure 2A, we explore the tilt angle formed by the Pb-X-Pb bonds as a function of temperature, where X denotes the halide. The Pb-X-Pb bond angle in the pseudo-cubic α phase has a value of $\sim 176^\circ$. As the temperature is reduced between 275 K and 250 K we clearly observe a gradual tilting of the Pb-X-Pb bond, with the angle reducing to between $161^\circ < x < 170^\circ$ as the structure adopts a pseudo-tetragonal β phase. We note that Fabini and coworkers studied the structure of the perovskite FAPbI₃ as a function of temperature, observing a similar gradual change in Pb-I-Pb bond angle for the α to β phase transition. Fabini *et al.* also found that as the rate of change of this angle decreased, the FAPbI₃ perovskite subsequently underwent a β to γ phase transformation.^[29] This is in contrast to the results shown in Figure 2B, where the bond angle gently plateaus after the phase transformation; this result is suggestive of a stabilisation of the β phase over a larger temperature range.

Using our structural model, we have also determined the unit cell parameters along the a , b and c axes as a function of temperature from the experimental data, as shown in Figure S4 (Supporting Information). This figure also shows the volume of a single lead-halide octahedron, plotted as a function of temperature. We can use the linear change in the octahedral volume to determine the volumetric thermal expansion coefficient (α_V) of the different perovskite phases. Here, we find that α_V in the α phase is around $154 \times 10^{-6} \text{ K}^{-1}$. However in the β phase, α_V could best be described by a second order polynomial, suggesting a dramatic change in the thermal expansion coefficient; this result is consistent with the presence of additional processes driving the expansion which accompany

changes in bond length – for example changes in the Pb-X-Pb bond angles. When we separate the volumetric thermal expansion into linear thermal expansion along the different crystal axes, we find that changes in the a -axis appear linear with temperature, whereas changes in the c -axis define the non-linear shape observed in the volumetric expansion shown in Figure S4.

Figure 2B plots the ratio $c\sqrt{2}/a$ as a function of temperature, where a and c are lattice parameters along the a and c axes. In comparing the cubic and tetragonal unit cells the c/a ratio is fundamental to differentiating these systems. In this case we use the reduced lattice parameter ratio $c\sqrt{2}/a$, where the scaling factor of $\sqrt{2}$ is included to make the lattice parameters of the cubic unit cell comparable to those of the tetragonal unit, which is based on the modelled two-octahedra unit cell. It can be seen that $c\sqrt{2}/a$ has a complex dependence on temperature, but apparently reaches a minimum around 200-220 K on both cooling and re-heating. As the rotation of the PbX_6 octahedra occurs about the c -axis, it is expected that the $c\sqrt{2}/a$ ratio in the β phase will exceed unity in accordance with previous findings.^[29] In Figure 2B however we observe exactly the opposite, and this peculiarity requires further investigation—for example through neutron diffraction experiments, which should provide sensitivity to the contributions of the organic cations.

At 90 K upon heating the sample, there is a discontinuity observed in the Pb-X-Pb bond angle (Figure 2A), a process that is also accompanied by a sudden drop in the $c\sqrt{2}/a$ ratio as shown in Figure 2B. Interestingly, we also observe weak scattering features at $Q = 1.72, 1.83$ and 2.80 \AA^{-1} at this same temperature. This observation suggests a possible phase change between 80 and 90 K. We note that Weber and coworkers observed a low temperature γ phase during cooling of the β phase in a neutron diffraction study of FAPbI_3 , and this γ phase included additional weak peaks which were attributed to the FA being rotationally locked in a variety of positions.^[26] However the contribution of FA cations to the total scattering is insignificant compared to that of the PbX framework (see Figure S5 in the Supporting Information), therefore the orientation of the FA cation remains unresolvable here.

The origin of the weak additional peaks observed at 90 K is unclear, as we were unable to fit them with the Rietveld model. We find that these peaks persist on heating past the suggested γ to β phase change and up to ~ 220 K. During heating from 150 K to 220 K, the values of the $c\sqrt{2}/a$ ratio (Figure 2B) are lower than those observed on cooling. This temperature range apparently coincides with the region in which these unidentified peaks persist on re-heating. Furthermore, these additional peaks disappear around the temperature at which $c\sqrt{2}/a$ reaches its minimum value. It is possible that such hysteresis effects may be related to a restriction of movement in the structure, or may be caused

by the presence of an additional phase in the material associated with the unidentified peaks. The structural features associated with these peaks may have an energy barrier to their formation and/or to their assimilation into the tetragonal phase; such a phenomenon would explain the temperature difference between the appearance and disappearance of the unassigned peaks. It may also explain the thermal hysteresis in the peak broadening behaviour as discussed above.

2.2 Absorption and Photoluminescence

In this section, we report on the optical properties of a $(\text{FAPbI}_3)_{0.85}(\text{MAPbBr}_3)_{0.15}$ thin film, measured while the film was heated from 4 K to 300 K, with full experimental details given in the ‘Experimental Methods’ section.

We first discuss temperature-dependent absorbance and photoluminescence (PL) spectra as shown in Figure 3A and Figure 3B, respectively. Here it can be seen that the absorption edge undergoes a blueshift as temperature is increased from 4 K to 300 K, a process which is accompanied by a similar blueshift of the PL emission maximum. We have extracted the optical band gap from the photoluminescence spectra by applying a Jacobian transformation to the intensity data at each temperature and fitting a Gaussian function to the resultant emission peaks. Using this, the band gap is then determined by the mean of the Gaussian. We have additionally determined the band gap from the absorbance spectra for each temperature using Tauc plots.^[30] We note here that there is likely to be a systematic error in the energy-value of the band edge determined here, due to the contribution of excitonic absorption to the absorbance spectrum as described by Elliott’s theory of excitons.^[31]

We plot the temperature-dependent optical band gap determined using both experimental methods in Figure 3C. Here it can be seen that the optical band gap as determined from the PL emission spectra undergoes an increase of ~ 34 meV over the entire temperature range. Interestingly, the band gap increase is not monotonic across the whole temperature range, but rather it reaches a local maximum at ~ 260 K and then reduces slightly up to ~ 280 K, where it begins to increase again. This behaviour is also apparent in the temperature-dependent band edge values extracted from the optical absorbance, where a discontinuity in the trend is observed at ~ 270 K. Another notable feature of the band gap variation is a small change in gradient at ~ 90 -100 K.

The empirical Varshni relation is generally used to describe the evolution of the band gap (E_g) of a semiconductor with temperature (T), with many semiconductors exhibiting a reduction in band gap with increasing temperature as a result of electron-phonon interactions and lattice expansion. The Varshni relation is as follows:

$$E_g(T) = E_g(T = 0) - \frac{\alpha T^2}{T + \beta} \quad (1)$$

where α and β are material constants.^[32] Clearly the positive value of dE_g/dT that we observe in this perovskite is inconsistent with the Varshni relation, with similar behaviour being reported previously in MAPbI₃.^[33;34] Recent calculations show that this is a result of the reduction in the overlap of Pb-6s and I-5s orbitals, which causes a decrease in the valence band maximum as the lattice expands.^[35;36]

Our measurements show that the band gap energy undergoes a slight redshift above 260 K, and the blueshift resumes at ~ 280 K. This discontinuity is indicative of a temperature range in which a structural phase transition occurs, with this effect observed in previous studies on a range of different perovskite compositions.^[27;37] For example, Zheng and coworkers reported a redshift in E_g of (FAPbI₃)_{0.8}(MAPbI₃)_{0.2} between 100 K and 160 K which they attributed to a phase transition occurring gradually between the low temperature orthorhombic and the intermediate tetragonal phases.^[38]

As detailed in Section 2.1, our PXRD measurements have revealed that, when cooling the sample, there is a high temperature phase transition from the pseudo-cubic phase to a tetragonal β phase at 260 K, and a low temperature phase transition that occurs between 80 K and 90 K. Upon reheating of the sample past 90 K, an intermediate structural configuration forms and is present up to 210-220 K, resulting in a deviation from the trend in lattice parameters observed upon cooling (see Figure 2B). Between 220 K and 260 K we observe the same tetragonal β phase as observed upon cooling. To compare trends in spectroscopic parameters with these temperature ranges, we mark these key temperatures on the plots in Figure 3; the blue vertical lines indicate 90 K, the red lines indicate 220 K and the black lines indicate 260 K. We deduce that the redshift observed in the band gap above 260 K is likely to be a result of this high temperature transition into the cubic phase. We also postulate that the non-linearity of the blueshift at lower temperatures may be correlated with the low temperature phase transition, as the change in gradient occurs at ~ 90 -100 K.

We plot the temperature-dependent absorbance spectra at selected temperatures in Figure S6 (Supporting Information). Here it is apparent that there is an excitonic-like absorption peak located just below the band edge at low temperatures, which is a well-documented phenomenon in the hybrid perovskite material family.^[39;2] This begins to flatten at ~ 90 K, which is the temperature at which we observe the low temperature γ to β structural phase transition in the PXRD data. We postulate that this excitonic feature appears as a result of this low temperature phase transition, as the exciton binding energy in the low temperature phase is larger than $k_B T$ over this temperature range (4-90 K). A similar effect has previously been observed in MAPbI₃ as it transforms to a low temperature

orthorhombic phase.^[40]

Figure 3D shows the temperature dependence of the Stokes shift, which has been plotted as the difference between the band edge as determined from Tauc plots and the band gap as extracted from steady state PL emission spectra. It can be seen that the Stokes shift increases in an approximately linear fashion with increasing temperature, starting from 3.19 meV at 10 K. The Stokes shift reaches a maximum of 7.83 meV at 220 K, where the trend reverses, and continues to drop up to 300 K. We note that the Stokes shift can provide a measure of the proportion of the PL emission that originates from sub-bandgap states,^[41] therefore a large Stokes shift would suggest a very disordered or defect-ridden material. In general, the distribution of sub-bandgap states decreases exponentially below the band edge, therefore if the participation of these states in the emission is temperature-dependent, then the Stokes shift is likely to follow an exponential distribution (with some associated activation energy). The observed Stokes shift is non-exponential, therefore we speculate that it is more likely to be influenced by polaronic effects,^[42] as detailed below.

It has been found in hybrid perovskites that photoexcitation causes significant lattice deformation,^[43] and therefore photoexcited electrons or holes may be localised by their own distortion field,^[44] giving rise to self-trapped electrons (STEs) or holes, which then may form small polarons through Fröhlich interactions with LO phonons.^[45;46] These interactions have been shown to lead to an elevated Stokes shift in lead halide and perovskite structures.^[47;48] Here we find that the Stokes shift-temperature gradient reverses at 220 K, a temperature which coincides with a change in the temperature gradient of the ratio $c\sqrt{2}/a$ on heating of the material (see Figure 2B). This correlation suggests that the Stokes shift is influenced by the shape and size of the unit cell. This observation supports our hypothesis that polaronic effects are the origin of the temperature dependence of the Stokes shift, because the shape of the unit cell will affect its polarisation and therefore influence the interaction between STEs and phonons.

We note that the broadening of the emission linewidth with increasing temperature that is observed in Figure 3B is consistent with other observations in hybrid lead halide perovskites.^[33;49;35] It has been proposed that the dominant mechanism for these broadening effects is Fröhlich coupling of photoexcited charge carriers with LO phonon modes.^[50;51] We believe that these polaronic effects, originating from Fröhlich interactions between self-trapped electrons and phonon modes, are consistent with our observation of a Stokes shift which increases with temperature.

Figure 3E plots the CW integrated PL emission intensity derived from Figure 3B. It can be seen that there is a near logarithmic decrease in the PL intensity with increasing temperature. This de-

crease in intensity indicates the activation of a series of thermally-induced non-radiative recombination centres as the film is heated.^[52;53] Interestingly, there is a departure from this trend at ~ 260 K, with the PL intensity increasing with increasing temperature. This temperature apparently coincides with the transition from the tetragonal β phase to the pseudo-cubic α phase observed in the PXRD data. This observation suggests a reduction in non-radiative recombination rates in the pseudo-cubic phase.

2.3 Recombination Dynamics

Recombination dynamics in photovoltaic cells are governed by three different recombination pathways, each of which depends to a different degree on the charge carrier density in the conduction band, n . The rate of change of n is given by:^[54]

$$\frac{dn}{dt} = -k_3n^3 - k_2n^2 - k_1n \quad (2)$$

The constant k_1 describes the rate of monomolecular recombination. In the perovskite MAPbI₃ it has been shown that the predominant monomolecular process is trap-assisted recombination, because the exciton binding energy of hybrid perovskites at room temperature is significantly lower than the thermal energy.^[55] The rate constant k_2 corresponds to bimolecular processes such as electron-hole recombination, which are more heavily dependent on the charge carrier density. In the hybrid perovskites investigated here, we expect this to be largely radiative recombination of free electrons and holes, as the dominant species in MAPbI₃ at room temperature has been shown to be free carriers.^[56] The third order constant k_3 is the Auger rate constant, which describes the rate of any three-body recombination process mediated either by a third charge carrier or a phonon.

In this study we used a streak camera to obtain time-resolved photoluminescence (TRPL) data, at a series of temperatures from 77 K to 315 K, using a pulsed laser focussed onto the sample with a resultant excitation fluence of $3.1 \mu\text{Jcm}^{-2}$. Full streak camera data shown in the Supporting Information (Figure S7) indicates a broadening in the emission peak with increasing temperature, a finding that is in agreement with the steady state PL data obtained from continuous wave measurements (see Figure 3B). Another key observation from this data is an increase in the apparent PL lifetime as we raise the temperature from 77 K to 200 K, followed by a decrease which continues up to ~ 290 K. This suggests that there is a decrease in the radiative recombination efficiency as the temperature is raised up to 200 K, with a subsequent increase in this quantity at higher temperatures.

We also analysed the temperature dependence of the PLQY to supplement our findings. The PLQY of the thin films was measured using an integrating sphere at room temperature, with PL

excited with a pulsed laser at $\sim 3 \mu\text{Jcm}^{-2}$, i.e. the same fluence we used for the TRPL measurements. The sample was then transferred to a cryostat and time-integrated PL emission was collected with a streak camera, at the same set of temperatures used for the TRPL measurements, again at a fluence of $\sim 3 \mu\text{Jcm}^{-2}$. By scaling the room temperature PLQY value to temperature-dependent values of the integral PL, we obtained the PLQY as a function of temperature (see Supplementary Note 2 in the Supporting Information for details). Figure 4A plots the PLQY of the film determined as a function of temperature. It can be seen that the PLQY is effectively constant at temperatures up to 100 K, but then decreases up to ~ 270 K, after which it undergoes an increase up to 315 K. These results are consistent with changes in bimolecular radiative recombination rates as we demonstrate below, although there may also be contributions to such effects from changes in non-radiative processes.

2.3.1 Bimolecular Recombination Rates

To analyse the TRPL streak camera images, we have selected data at a time delay of < 1600 ps by averaging time-resolved PL intensity data across the central two-thirds of the peak emission spectrum. We utilised rate equation (2) to attempt to quantify the bimolecular recombination rate k_2 as a function of temperature. Here we consider a simplified version of Equation (2) given by:

$$\frac{dn}{dt} = -k_2n^2 - k_1n \quad (3)$$

Buizza *et al.* [57] recently presented an analytical solution to this modified form of the rate equation, which is as follows:

$$n(t) = \frac{k_1\alpha}{e^{k_1t} - \alpha k_2} \quad \text{for} \quad \frac{1}{\alpha} = \frac{k_1}{n_0} + k_2 \quad (4)$$

where n_0 is the initial charge carrier density. This model assumes that the charge carrier density is low enough such that Auger recombination has a negligible effect on the PL emissions. The TRPL data presented here was collected at a laser excitation fluence of $\sim 3 \mu\text{Jcm}^{-2}$, which corresponds to an initial charge carrier density of $n_0 \sim 10^{17} \text{ cm}^{-3}$ in the $(\text{FAPbI}_3)_{0.85}(\text{MAPbBr}_3)_{0.15}$ film. It has been shown in lead halide perovskites that PL signal is proportional to n^2 at excitation densities in the region $10^{17} < n_0 < 10^{18}$, demonstrating that bimolecular recombination dominates the PL dynamics at these fluences and that Auger processes make a negligible contribution. [58]

Using the approximation that the PL signal is proportional to n^2 , [59] we scaled the PL decay traces using the relation $n(t) = \sqrt{\frac{I(t)}{I_0}}n_0$ where $I(t)$ is the time dependence of the PL intensity. A selection

of data processed in this way is shown in Figure 4B, where we plot the charge carrier density as a function of time at a selection of different temperatures. In order to obtain estimates of k_2 , we fitted the $n(t)$ curves to Equation (4). To obtain an estimate for the temperature-dependent monomolecular rate k_1 , we collected TRPL traces at low fluence ($\sim 30 \text{ nJcm}^{-2}$) via TCSPC measurements, at a series of temperatures from 77 K to 300 K (see Figure S8 in the Supporting Information). At such a low excitation fluence (equivalent to a photoexcited carrier density of $n_0 \sim 10^{15} \text{ cm}^{-3}$), the density of electron traps will be much larger than the concentration of photoexcited electrons. A consequence of this is that electron-hole recombination is almost monomolecular and is solely determined by the rate of trapping, and thus the PL decay rate reflects the monomolecular recombination rate k_1 .^[60] We therefore fitted these traces to an exponential model (see Supplementary Note 3 in the Supporting Information for full details) to obtain approximate values for k_1 , which were in the range $\sim 1\text{-}3 \times 10^6 \text{ s}^{-1}$ at all temperatures, which is in good agreement with previous studies on similar hybrid perovskites.^[61;62] These values of k_1 , which correspond to lifetimes on the order of 100s of ns, will have a negligible effect on the TRPL dynamics, because the streak camera only probes time dynamics up to a maximum delay of 1.6 ns. As a result, we fix k_1 at 10^6 s^{-1} for all temperatures.

Fits to the data from the analytical solution expressed in Equation (4) are shown as dashed black lines in Figure 4B. We have also extracted k_2 values using a linearised version of Equation (4), using a similar method to that of Shaw *et al.*, who analysed the bimolecular process of exciton-exciton annihilation.^[63] Linearised data and fits are shown in Figure 4C. Our extracted value of k_2 at room temperature is $9.98 \times 10^{-10} \text{ cm}^3\text{s}^{-1}$, which is in reasonable agreement with reported values of k_2 in hybrid perovskites: $1.1 \times 10^{-10} \text{ cm}^3\text{s}^{-1}$ (FAPbI₃); $11 \times 10^{-10} \text{ cm}^3\text{s}^{-1}$ (FAPbBr₃);^[62] and $9.2 \times 10^{-10} \text{ cm}^3\text{s}^{-1}$ (MAPbI₃).^[64] The temperature dependence of the quantity k_2 , as extracted from fits to the analytical solution, is shown in Figure 4D. Starting from 77 K, we find that k_2 decreases with increasing temperature, and reaches a minimum value at around 200 K. This trend in k_2 is consistent with previous experimental and theoretical results presented for MAPbI₃ over this temperature range.^[21;64] Above 200 K, k_2 increases and reaches a maximum value at 290 K, from which point it again undergoes a decrease as temperature is increased to 315 K. Values of k_2 from the linearised model show very good agreement with those extracted from the analytical solution, but there is increased scatter in the data above 260 K, suggesting that the model employed here does not fully describe the PL dynamics in this temperature range—most likely resulting from higher order recombination processes for which the model cannot account.

Interestingly, we find that the decrease in PLQY observed as the temperature is increased to 200 K

(Figure 4A) correlates with decreasing bimolecular rates, however above this temperature, the PLQY continues to decrease up to ~ 280 K while we see an apparent increase in k_2 . This suggests it is not just bimolecular recombination rates that affect the quantum yield over this temperature range, but that higher order non-radiative processes also become important.

We suspect that the observed reduction in k_2 with increasing temperature between 100 K and 200 K, and again between 290 K and 315 K, may result from a decrease in charge carrier mobility within the framework of the Langevin model. Indeed, it is known that a decrease in electron mobility occurs on increasing temperature in hybrid lead halide perovskites.^[65;66] Such reduced carrier mobility will reduce the likelihood that electrons and holes will move within each other's joint Coulomb capture radii, thereby reducing the bimolecular recombination rate.

The Langevin model has however been shown to overestimate k_2 in hybrid lead halide perovskites,^[33;67] and thus this theory is not sufficient to predict temperature-dependent recombination rates. Recent theoretical work has used the Shockley-van Roosbroeck relation,^[68] which describes the radiative recombination rate as a function of temperature using the following:

$$R_{RAD} = \int_0^{\infty} \rho(E, T)P(E, T)dE \quad (5)$$

where $\rho(E, T)dE$ is the density of photons in the material in the interval dE , and $P(E, T)dE$ is the probability per unit time that a photon of energy E is absorbed.^[64] The quantity R_{RAD} can then be used to find the bimolecular recombination rate k_2 , which is predicted to decrease with increasing temperature due to the thermal broadening of the Fermi-Dirac and Bose-Einstein distribution functions. In Figure 4D we observe a decrease of k_2 on heating the sample from 100 K to 200 K, and thus we conclude that over this temperature range, changes in the recombination rate are indeed dominated by changes in bimolecular recombination. However, this trend does not hold across the entire temperature range, as we observe an increase in k_2 at temperatures between ~ 200 K and ~ 290 K. This suggests that, in this temperature region, there is a second effect that competes with the thermal broadening effects and determines the overall recombination rates.

To explore the origin of this competing effect, we revisit our temperature-dependent structural parameters shown in Figure 2, which we determined from Rietveld fits to PXRD data. It can be seen in Figure 2B that the lattice parameter ratio $c\sqrt{2}/a$ reaches a minimum at ~ 200 - 220 K on heating, and subsequently increases up to 260 K, where it stabilises again. If we compare this to temperature-dependent trends in k_2 , we observe that this rate also reaches a minimum at ~ 200 K. As was shown earlier, the magnitude of the Stokes shift is also influenced by such changes in structural configuration,

with this effect most likely to result from polaronic effects rather than from changes in the distribution of sub-bandgap states. Therefore we suggest that polaronic effects arising from structural changes on heating of the sample are responsible for the deviation of k_2 from the trend predicted by the Shockley-van Roosbroeck model between 200 K and 290 K. One possible mechanism for this is defect tolerance induced by the formation of large polarons.^[69]

3 Conclusions

In summary, we have presented experimental evidence for two structural phase transitions occurring in $(\text{FAPbI}_3)_{0.85}(\text{MAPbBr}_3)_{0.15}$ upon cooling and heating between 350 K and 80 K. The material exists in a pseudo-cubic α phase at room temperature, and transforms to a pseudo-tetragonal β phase at around 260 K. We also present evidence for the occurrence of a low temperature phase transition at approximately 80-90 K, where the material assumes a structure which can be most accurately described as a variation on the tetragonal phase with reduced symmetry. Our identification of such transitions is based on an analysis of temperature-dependent changes in structural parameters such as the Pb-X-Pb tilt angle and unit cell volume, which have been determined from Rietveld refinements applied to the XRD data. The β phase appears to stabilise over a large temperature range. The reduced lattice parameter ratio $c\sqrt{2}/a$ exhibits a complex temperature dependence which may suggest an intermediate structural configuration or the presence of an additional phase in the 100-220 K region.

We have observed that the optoelectronic properties of this material depend strongly on temperature, exhibiting trends that correlate with identified phase transitions and other changes in structural configuration. We have shown that the integrated PL intensity is correlated with the phase behaviour, with this quantity increasing by $\sim 60\%$ when the material undergoes a phase transition to the pseudo-cubic perovskite phase. Our measurements also reveal a complex dependence of the Stokes shift on temperature, and this trend correlates with changes in the reduced lattice parameter ratio $c\sqrt{2}/a$.

Furthermore, we have demonstrated that bimolecular recombination rates in this material have a negative temperature gradient in the pseudo-tetragonal phase up to ~ 200 K, which is consistent with the predictions of the Shockley-van Roosbroeck model for radiative recombination. At a temperature of ~ 200 K, this trend reverses, coinciding with changes in the lattice parameter ratio $c\sqrt{2}/a$ as determined from temperature-dependent PXRD data. We have suggested that these changes in crystal structure lead to polaronic effects which compete with the thermal broadening as described by Shockley-van Roosbroeck in determining recombination rates. We therefore propose, with evidence from steady state and time-resolved PL data, that changes in the size and shape of the unit cell alter

the emission properties, and suggest that this may be due, at least in part, to polaron formation in the material.

Finally, we note that the observed high temperature phase transition to the pseudo-cubic perovskite phase is within the expected operating temperature range of a photovoltaic cell, when used under outdoor conditions. This will clearly affect the photovoltaic performance of cells based on $(\text{FAPbI}_3)_{0.85}(\text{MAPbBr}_3)_{0.15}$, through its effect on the band gap (and therefore the available V_{OC}). Encouragingly however, the low temperature of the tetragonal-cubic phase transition relative to MAPbI_3 makes this material more thermally stable—a property that will be advantageous to long-term stable photovoltaic cell operation.

4 Experimental Methods

Materials Fabrication: MAPbBr_3 solution (1.3 M) was made by dissolving MABr (Greatcell) and PbBr_2 (TCI UK Ltd.) in a 4:1 mixture of anhydrous N,N -dimethylformamide (DMF) to anhydrous dimethyl sulfoxide (DMSO) (Sigma Aldrich). FAPbI_3 solution (1.3 M) was also made by dissolving FAI (Greatcell) and PbI_2 (99.99%, TCI UK Ltd.) in a 4:1 DMF:DMSO mixture. Next the FAPbI_3 solution (0.85 mL) and the MAPbBr_3 solution (0.15 mL) were mixed to give the desired composition.

The solution was then thoroughly vortex-mixed, before being syringe filtered and spread onto a synthetic quartz-coated substrate that had been cleaned and UV-ozone treated. The solution was then spin-coated according to the following regime: substrate was accelerated from 0 to 2000 rpm at 200 rpm s^{-1} , then held at 2000 rpm for 10 s. It was then accelerated from 2000 to 6000 rpm at 2000 rpm s^{-1} , and held at 6000 rpm for 20 s. An antisolvent quench of 100 μL of anhydrous chlorobenzene (Sigma Aldrich) was dripped onto the film 10 s before the end of this final step. The film was then heated at 100°C for 30 minutes.

Powder X-Ray Diffraction Measurements: Thin film samples were prepared via the protocol above and scraped from the substrate using a razor blade; the resultant fine powder was loaded into a 0.7 mm borosilicate capillary. Powder diffraction data were obtained using a Bruker D8 Advance powder diffractometer using $\text{CuK}\alpha$ radiation and equipped with focusing Göbel mirrors and a high resolution energy-dispersive Lynxeye XE detector. Data were collected in a Debye-Scherrer geometry with rotating capillary stage. Sample temperature for in situ heating studies was controlled by a co-axial stream of dry nitrogen gas from an Oxford Cryosystems Cryostream 700 Plus, with a flow rate of 5 L/min.

Powder X-Ray Diffraction Modelling: Structural information modelling of the variable temperature

powder X-ray diffraction (PXRD) data was performed primarily using structure model based Rietveld refinements with a fundamental parameters (FP) approach. FP involves refining an instrument profile to describe the intensity and broadening characteristics of the diffractometer used. This allows greater accuracy of the peak positions and uses fewer free parameters, improving the stability of the refinements. The instrument profile was refined against a silicon standard. The space group assignments made are based on the symmetry of the PbX_6^{4-} octahedra.

The model used in the Rietveld refinements employed a model based on the $P4/mbm$ space group in which the halide mixture (substitution) has been accounted for using site occupancy factors; this assumes that the different halides are uniformly distributed across the halide sites. The contribution of the organic cations to the PXRD pattern is minimal as seen in Figure S5 (Supporting Information), thus the effect of the 15% MA on the diffraction pattern was considered negligible. FA was excluded from the symmetry constraints of the phases. Pb was allowed movement in the ab -plane by adjusting site occupancies and replicating Pb as per the $P4$ symmetry. The refinements were performed using TOPAS v5 (Bruker) The data was fitted using Monte-Carlo assisted sequential Rietveld refinements with TOPAS v5 (Bruker). Along with the symmetry constraints of the model this method was essential in stabilising the refinements.

Analytical Pearson VII functions^[70] were applied in separate refinements which can be found in the Supporting Information (Figure S3). The Pearson VII fits provide a more direct observation of the changes in apparent peak position and width.

Absorption and Steady State Photoluminescence: For absorption measurements, samples were illuminated with a deuterium-halogen lamp (Ocean Optics) and transmitted light was collected in an optical fibre and passed to an Ocean Optics HR2000+ES spectrometer to obtain spectral data. For PL measurements, samples were illuminated with a 405 nm CW laser at 800 μW in reflection mode and PL emissions were collected in the aforementioned spectrometer. Samples were cooled to 4 K using an Oxford Instruments OptistatDry cryostat, and absorption and PL measurements were taken at regular intervals as the system was heated back to room temperature.

Streak Camera Measurements: The samples were excited with 515 nm wavelength pulses of 200 fs duration generated from the second harmonic of a regeneratively amplified femtosecond laser system (Pharos from Light Conversion) with a repetition rate of 100 kHz. The excitation spot diameter was 175 μm . The emitted light was resolved spectrally using a Princeton Instruments Acton SpectraPro SP-2300 spectrograph, and temporally using a Hamamatsu Streak camera (C10600 Orca-R2 coupled to a M10911 synchroscan unit). Samples were cooled by liquid nitrogen in a bath cryostat.

Photoluminescence Quantum Yield: The photoluminescence quantum yield (PLQY) was measured by using 200 fs duration 515 nm laser pulses at 100 kHz (Pharos from Light Conversion) focused to a 175 μm spot diameter on the sample in an integrating sphere. The emitted light was collected using an optical fiber and spectrally resolved using an Oriel Instruments 77400 spectrometer coupled to an Andor iDUS420-BV CCD camera. The spectral sensitivity of the system was scaled using a calibrated quartz tungsten halogen lamp Bentham CL6-H. The room temperature PLQY was obtained using the method described by de Mello *et al.*^[71] Temperature-dependent time-integrated PL emission was recorded using a Hamamatsu streak camera with the same excitation density as that used for the PLQY measurement, with the sample cooled using a bath cryostat.

Low Fluence TCSPC Measurements: The samples were illuminated with a 507 nm pulsed laser (PicoQuant-LDH-510-C) operating at 2.5 MHz with a maximum time delay of 350 ns. Timing electronics were controlled through a TimeHarp 260 (PICO) PCIe board with a time resolution of 100 ps. Photoluminescence was detected with a silicon SPAD (single-photon avalanche diode) detector, without wavelength selection. For temperature-dependent measurements, samples were cooled in an Oxford Instruments MicroStat with continuous flow liquid helium and the sample temperature was monitored by an Oxford Instruments temperature controller.

Crystallographic data

Crystallographic data (excluding structure factors) for the structure(s) reported in this paper have been deposited with the Cambridge Crystallographic Data Centre as supplementary publication no. CCDC 1898355-1898366. Copies of the data can be obtained free of charge from www.ccdc.cam.ac.uk/conts/retrieving or on application to The Director at the following address: Cambridge Crystallographic Data Centre (CCDC), 12 Union Road, Cambridge CB2 1EZ, UK.

Supporting Information

Supporting Information is available from the Wiley Online Library or from the author.

Acknowledgements

C.G. and J.A.S. would like to thank the UK EPSRC for funding their PhD studentships via the Centre for Doctoral Training in “New and Sustainable Photovoltaics” (EP/L01551X/1). We also

thank the UK STFC and EPSRC for part-funding this work via grants ST/R002754/1 “Synchrotron Techniques for African Research and Technology” and “Hybrid Polaritonics” (EP/M025330/1). A.S. hereby acknowledges the financial assistance of the South Africa National Research Foundation (NRF), University of the Witwatersrand - Material and Energy Research Group (MERG) and DST-NRF Centre of Excellence in Strong Materials (CoE-SM) towards this research. Opinions expressed and conclusions arrived at are those of the author and are not necessarily to be attributed to the funding organisations.

The authors gratefully acknowledge Dr. Craig C. Robertson from the Department of Chemistry at the University of Sheffield for collecting the PXRD data. C. G. would also like to thank Dr. David Coles and Dr. Kyriacos Georgiou for help with photoluminescence quantum yield measurements.

Conflict of Interest

D.G.L. is a director of the company Ossila Ltd that retails materials and equipment used in perovskite photovoltaic research.

References

- [1] NREL: Best Research-Cell Efficiencies Chart, accessed at <https://pvdpc.nrel.gov/>, **2019**.
- [2] V. D’Innocenzo, G. Grancini, M. J. P. Alcocer, A. R. S. Kandada, S. D. Stranks, M. M. Lee, G. Lanzani, H. J. Snaith, A. Petrozza, *Nat. Commun.* **2014**, *5*, 3586.
- [3] S. D. Stranks, G. E. Eperon, G. Grancini, C. Menelaou, M. J. P. Alcocer, T. Leijtens, L. M. Herz, A. Petrozza, H. J. Snaith, *Science (New York, N.Y.)* **2013**, *342*, 341.
- [4] C. Wehrenfennig, G. E. Eperon, M. B. Johnston, H. J. Snaith, L. M. Herz, *Adv. Mater.* **2014**, *26*, 1584.
- [5] K. X. Steirer, P. Schulz, G. Teeter, V. Stevanovic, M. Yang, K. Zhu, J. J. Berry, *ACS Energy Lett.* **2016**, *1*, 360.
- [6] K. Hwang, Y.-S. Jung, Y.-J. Heo, F. H. Scholes, S. E. Watkins, J. Subbiah, D. J. Jones, D.-Y. Kim, D. Vak, *Adv. Mater.* **2015**, *27*, 1241.
- [7] J. E. Bishop, D. K. Mohamad, M. Wong-Stringer, A. Smith, D. G. Lidzey, *Sci. Rep.* **2017**, *7*, 7962.

- [8] A. Kojima, K. Teshima, Y. Shirai, T. Miyasaka, *J. Am. Chem. Soc.* **2009**, *131*, 6050.
- [9] W. Tress, N. Marinova, O. Inganäs, M. K. Nazeeruddin, S. M. Zakeeruddin, M. Grätzel, *Adv. Energy Mater.* **2015**, *5*, 1400812.
- [10] B. Conings, J. Drijkoningen, N. Gauquelin, A. Babayigit, J. D'Haen, L. D'Olieslaeger, A. Ethirajan, J. Verbeeck, J. Manca, E. Mosconi, F. D. Angelis, H.-G. Boyen, *Adv. Energy Mater.* **2015**, *5*, 1500477.
- [11] G. E. Eperon, S. D. Stranks, C. Menelaou, M. B. Johnston, L. M. Herz, H. J. Snaith, *Energy Environ. Sci.* **2014**, *7*, 982.
- [12] N. Pellet, P. Gao, G. Gregori, T.-Y. Yang, M. K. Nazeeruddin, J. Maier, M. Grätzel, *Angew. Chem.* **2014**, *126*, 3215.
- [13] T. Jesper Jacobsson, J.-P. Correa-Baena, M. Pazoki, M. Saliba, K. Schenk, M. Grätzel, A. Hagfeldt, *Energy Environ. Sci.* **2016**, *9*, 1706.
- [14] W. S. Yang, J. H. Noh, N. J. Jeon, Y. C. Kim, S. Ryu, J. Seo, S. I. Seok, *Science* **2015**, *348*, 1234.
- [15] N. J. Jeon, J. H. Noh, W. S. Yang, Y. C. Kim, S. Ryu, J. Seo, S. I. Seok, *Nature* **2015**, *517*, 476.
- [16] D. Bi, W. Tress, M. I. Dar, P. Gao, J. Luo, C. Renevier, K. Schenk, A. Abate, F. Giordano, J.-P. Correa Baena, J.-D. Decoppet, S. M. Zakeeruddin, M. K. Nazeeruddin, M. Grätzel, A. Hagfeldt, *Sci. Adv.* **2016**, *2*, e1501170.
- [17] E. Skoplaki, A. Boudouvis, J. Palyvos, *Sol. Energy Mater. Sol. Cells* **2008**, *92*, 1393.
- [18] L.-Q. Xie, L. Chen, Z.-A. Nan, H.-X. Lin, T. Wang, D.-P. Zhan, J.-W. Yan, B.-W. Mao, Z.-Q. Tian, *J. Am. Chem. Soc.* **2017**, *139*, 3320.
- [19] O. J. Weber, B. Charles, M. T. Weller, *J. Mater. Chem. A* **2016**, *4*, 15375.
- [20] G. Kieslich, J. M. Skelton, J. Armstrong, Y. Wu, F. Wei, K. L. Svane, A. Walsh, K. T. Butler, *Chem. Mater.* **2018**, *30*, 8782.
- [21] R. L. Milot, G. E. Eperon, H. J. Snaith, M. B. Johnston, L. M. Herz, *Adv. Funct. Mater.* **2015**, *25*, 6218.
- [22] M. C. Gélvez-Rueda, N. Renaud, F. C. Grozema, *J. Phys. Chem. C* **2017**, *121*, 23392.

- [23] M. T. Weller, O. J. Weber, P. F. Henry, A. M. Di Pumpo, T. C. Hansen, *Chem. Commun.* **2015**, 51, 4180.
- [24] T. Chen, B. J. Foley, C. Park, C. M. Brown, L. W. Harriger, J. Lee, J. Ruff, M. Yoon, J. J. Choi, S.-H. Lee, *Sci. Adv.* **2016**, 2, e1601650.
- [25] M. T. Weller, O. J. Weber, J. M. Frost, A. Walsh, *J. Phys. Chem. Lett.* **2015**, 6, 3209.
- [26] O. J. Weber, D. Ghosh, S. Gaines, P. F. Henry, A. B. Walker, M. S. Islam, M. T. Weller, *Chem. Mater.* **2018**, 30, 3768.
- [27] H.-H. Fang, F. Wang, S. Adjokatse, N. Zhao, J. Even, M. Antonietta Loi, *Light: Sci. Appl.* **2016**, 5, e16056.
- [28] D. H. Fabini, T. A. Siaw, C. C. Stoumpos, G. Laurita, D. Olds, K. Page, J. G. Hu, M. G. Kanatzidis, S. Han, R. Seshadri, *J. Am. Chem. Soc.* **2017**, 139, 16875.
- [29] D. H. Fabini, C. C. Stoumpos, G. Laurita, A. Kaltzoglou, A. G. Kontos, P. Falaras, M. G. Kanatzidis, R. Seshadri, *Angew. Chem., Int. Ed.* **2016**, 55, 15392.
- [30] J. Tauc, *Mater. Res. Bull.* **1968**, 3, 37.
- [31] R. J. Elliott, *Phys. Rev.* **1957**, 108, 1384.
- [32] Y. Varshni, *Physica* **1967**, 34, 149.
- [33] K. Wu, A. Bera, C. Ma, Y. Du, Y. Yang, L. Li, T. Wu, *Phys. Chem. Chem. Phys.* **2014**, 16, 22476.
- [34] H.-H. Fang, R. Raissa, M. Abdu-Aguye, S. Adjokatse, G. R. Blake, J. Even, M. A. Loi, *Adv. Funct. Mater.* **2015**, 25, 2378.
- [35] M. I. Dar, G. Jacopin, S. Meloni, A. Mattoni, N. Arora, A. Boziki, S. M. Zakeeruddin, U. Rothlisberger, M. Grätzel, *Sci. Adv.* **2016**, 2, e1601156.
- [36] S. Meloni, G. Palermo, N. Ashari-Astani, M. Grätzel, U. Rothlisberger, *J. Mater. Chem. A* **2016**, 4, 15997.
- [37] E. S. Parrott, T. Green, R. L. Milot, M. B. Johnston, H. J. Snaith, L. M. Herz, *Adv. Funct. Mater.* **2018**, 28, 1802803.

- [38] H. Zheng, J. Dai, J. Duan, F. Chen, G. Zhu, F. Wang, C. Xu, *J. Mater. Chem. C* **2017**, *5*, 12057.
- [39] M. Hirasawa, T. Ishihara, T. Goto, *J. Phys. Soc. Jpn.* **1994**, *63*, 3870.
- [40] E. M. Hutter, M. C. Gélvez-Rueda, A. Osherov, V. Bulović, F. C. Grozema, S. D. Stranks, T. J. Savenije, *Nature Materials* **2017**, *16*, 115.
- [41] A. D. Wright, R. L. Milot, G. E. Eperon, H. J. Snaith, M. B. Johnston, L. M. Herz, *Adv. Funct. Mater.* **2017**, *27*, 1700860.
- [42] R. Williams, K. Song, *J. Phys. Chem. Solids* **1990**, *51*, 679.
- [43] R. Gottesman, E. Haltzi, L. Gouda, S. Tirosh, Y. Bouhadana, A. Zaban, E. Mosconi, F. De Angelis, *J. Phys. Chem. Lett.* **2014**, *5*, 2662.
- [44] E. T. Hoke, D. J. Slotcavage, E. R. Dohner, A. R. Bowring, H. I. Karunadasa, M. D. McGehee, *Chem. Sci.* **2015**, *6*, 613.
- [45] A. J. Neukirch, W. Nie, J. C. Blancon, K. Appavoo, H. Tsai, M. Y. Sfeir, C. Katan, L. Pedesseau, J. Even, J. J. Crochet, G. Gupta, A. D. Mohite, S. Tretiak, *Nano Lett.* **2016**, *16*, 3809.
- [46] D. Cortecchia, J. Yin, A. Bruno, S.-Z. A. Lo, G. G. Gurzadyan, S. Mhaisalkar, J.-L. Brédas, C. Soci, *J. Mater. Chem. C* **2017**, *5*, 2771.
- [47] V. Plekhanov, *Prog. Mater. Sci.* **2004**, *49*, 787.
- [48] K. Gauthron, J.-S. Lauret, L. Doyennette, G. Lanty, A. Al Choueiry, S. J. Zhang, A. Brehier, L. Largeau, O. Mauguin, J. Bloch, E. Deleporte, *Opt. Express* **2010**, *18*, 5912.
- [49] C. Wehrenfennig, M. Liu, H. J. Snaith, M. B. Johnston, L. M. Herz, *J. Phys. Chem. Lett.* **2014**, *5*, 1300.
- [50] A. D. Wright, C. Verdi, R. L. Milot, G. E. Eperon, M. A. Pérez-Osorio, H. J. Snaith, F. Giustino, M. B. Johnston, L. M. Herz, *Nat. Commun.* **2016**, *7*, 11755.
- [51] S. Ghosh, Q. Shi, B. Pradhan, P. Kumar, Z. Wang, S. Acharya, S. K. Pal, T. Pullerits, K. J. Karki, *J. Phys. Chem. Lett.* **2018**, *9*, 4245.
- [52] J. Kim, S.-H. Lee, J. H. Lee, K.-H. Hong, *J. Phys. Chem. Lett.* **2014**, *5*, 1312.
- [53] W.-J. Yin, T. Shi, Y. Yan, *Appl. Phys. Lett.* **2014**, *104*, 063903.

- [54] M. B. Johnston, L. M. Herz, *Acc. Chem. Res.* **2016**, *49*, 146.
- [55] J. Even, L. Pedesseau, C. Katan, *J. Phys. Chem. C* **2014**, *118*, 11566.
- [56] Y. Yamada, T. Nakamura, M. Endo, A. Wakamiya, Y. Kanemitsu, *J. Am. Chem. Soc.* **2014**, *136*, 11610.
- [57] L. R. V. Buizza, T. W. Crothers, Z. Wang, J. B. Patel, R. L. Milot, H. J. Snaith, M. B. Johnston, L. M. Herz, *Adv. Funct. Mater.* **2019**, 1902656.
- [58] M. Saba, M. Cadelano, D. Marongiu, F. Chen, V. Sarritzu, N. Sestu, C. Figus, M. Aresti, R. Piras, A. Geddo Lehmann, C. Cannas, A. Musinu, F. Quochi, A. Mura, G. Bongiovanni, *Nat. Commun.* **2014**, *5*.
- [59] F. Deschler, M. Price, S. Pathak, L. E. Klintberg, D.-D. Jarausch, R. Higler, S. Hu, T. Leijtens, S. D. Stranks, H. J. Snaith, M. Atatu, R. T. Phillips, R. H. Friend, *J. Phys. Chem. Lett* **2014**, *5*, 1421.
- [60] S. D. Stranks, V. M. Burlakov, T. Leijtens, J. M. Ball, A. Goriely, H. J. Snaith, *Phys. Rev. Appl.* **2014**, *2*, 034007.
- [61] D. P. McMeekin, G. Sadoughi, W. Rehman, G. E. Eperon, M. Saliba, M. T. Hörantner, A. Haghighirad, N. Sakai, L. Korte, B. Rech, M. B. Johnston, L. M. Herz, H. J. Snaith, *Science* **2016**, *351*, 151.
- [62] W. Rehman, R. L. Milot, G. E. Eperon, C. Wehrenfennig, J. L. Boland, H. J. Snaith, M. B. Johnston, L. M. Herz, *Adv. Mater.* **2015**, *27*, 7938.
- [63] P. E. Shaw, A. Ruseckas, I. D. Samuel, *Adv. Mater.* **2008**, *20*, 3516.
- [64] C. L. Davies, M. R. Filip, J. B. Patel, T. W. Crothers, C. Verdi, A. D. Wright, R. L. Milot, F. Giustino, M. B. Johnston, L. M. Herz, *Nat. Commun.* **2018**, *9*, 293.
- [65] H. Oga, A. Saeki, Y. Ogomi, S. Hayase, S. Seki, *J. Am. Chem. Soc.* **2014**, *136*, 13818.
- [66] T. J. Savenije, C. S. Ponseca, L. Kunneman, M. Abdellah, K. Zheng, Y. Tian, Q. Zhu, S. E. Canton, I. G. Scheblykin, T. Pullerits, A. Yartsev, V. Sundstro, V. Sundström, *J. Phys. Chem. Lett* **2014**, *5*, 4.

- [67] K. Tanaka, T. Takahashi, T. Ban, T. Kondo, K. Uchida, N. Miura, *Solid State Communications* **2003**, *127*, 619.
- [68] A. Filippetti, P. Delugas, A. Mattoni, *J. Phys. Chem. C* **2014**, *118*, 24843.
- [69] K. Miyata, D. Meggiolaro, M. T. Trinh, P. P. Joshi, E. Mosconi, S. C. Jones, F. De Angelis, X.-Y. Zhu, *Sci. Adv.* **2017**, *3*, e1701217.
- [70] R. Young (Ed.), *The Rietveld Method*, Oxford University Press, Oxford, UK, **1995**.
- [71] J. C. De Mello, H. F. Wittmann, R. H. Friend, *Adv. Mater.* **1997**, *9*, 230.

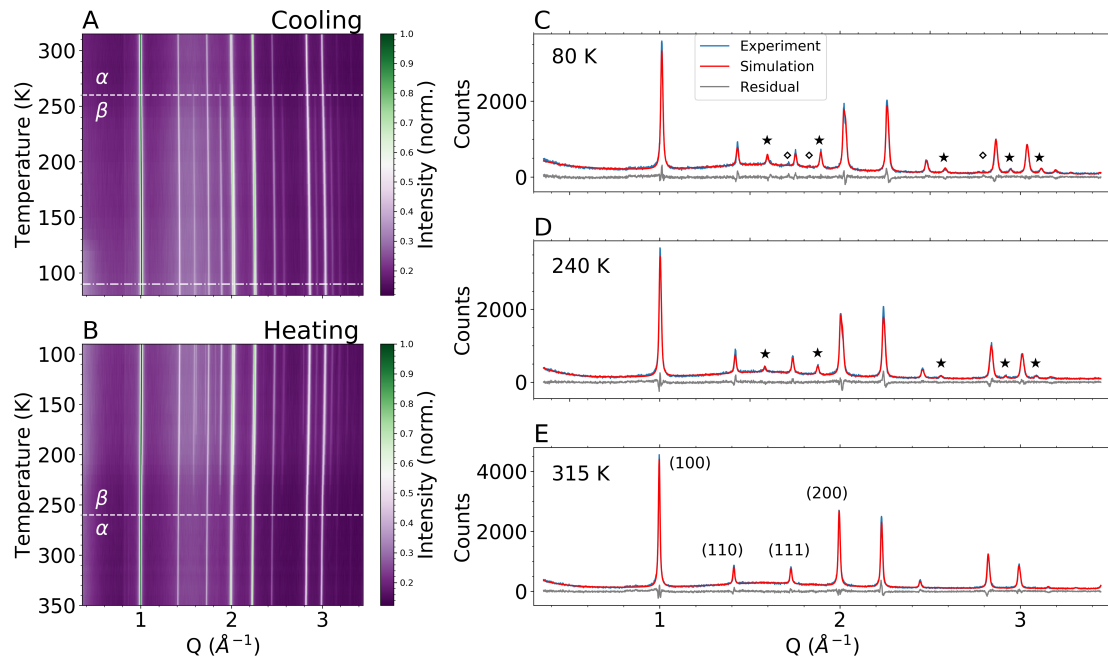


Figure 1: Variable temperature PXRD characterisation of powder samples of $(\text{FAPbI}_3)_{0.85}(\text{MAPbBr}_3)_{0.15}$. Temperature-dependent powder X-ray scattering measurements across a wide Q -range whilst **A** cooling from 315 K to 80 K and **B** heating from 90 K to 350 K. PXRD line profiles for the sample at **C** 80 K (in the proposed γ phase), **D** 240 K (representative of the intermediate β phase) and **E** 315 K (the high temperature pseudo-cubic α phase). Peaks marked \star denote peaks which are characteristic of the β phase; \diamond denotes further additional peaks which are characteristic of the γ phase, which have not been fitted with the structural model.

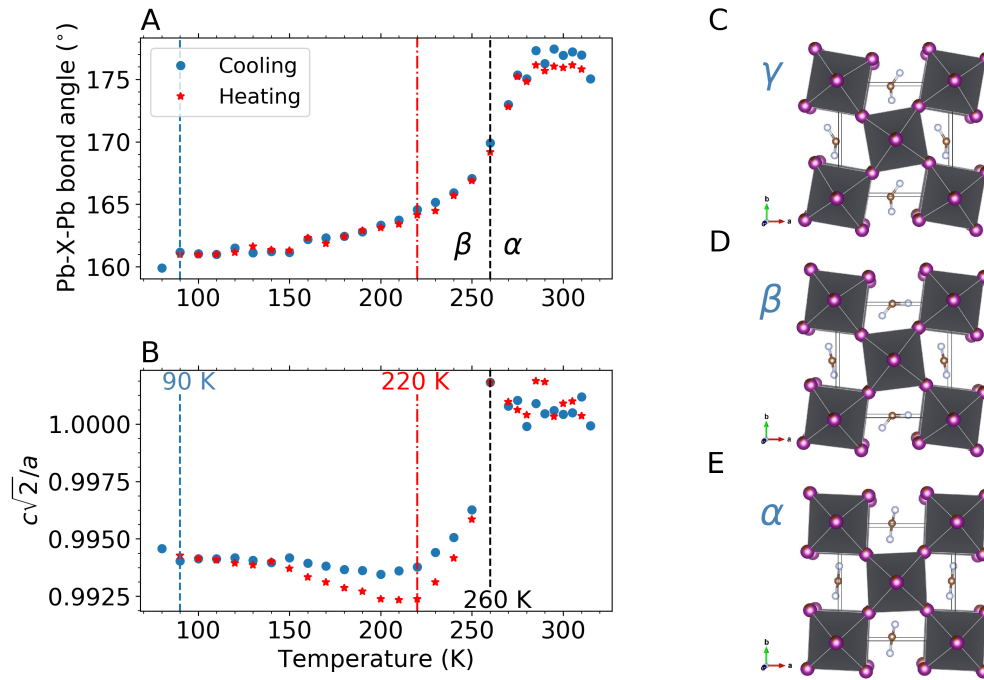


Figure 2: Temperature dependence of **A** the Pb-X-Pb bond angle and **B** the reduced lattice parameter ratio $c\sqrt{2}/a$. These parameters have been extracted from the Rietveld refinement model applied to the PXRD data, upon both heating and cooling of the sample. Proposed unit cells for the **C** γ phase (below 90 K), **D** β phase (pseudo-tetragonal, 90-250 K) and **E** α phase (pseudo-cubic, above 260 K), generated from the Rietveld models.

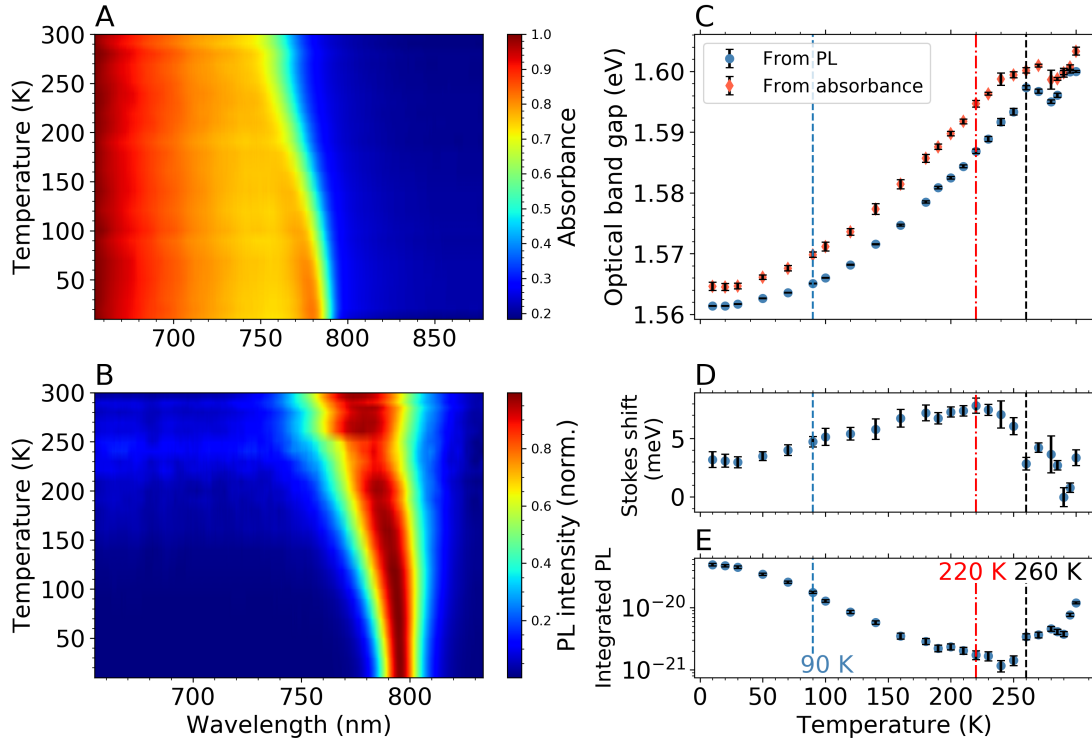


Figure 3: Temperature dependence of **A** the absorption spectra and **B** the PL spectra for $(\text{FAPbI}_3)_{0.85}(\text{MAPbBr}_3)_{0.15}$ perovskite thin films on heating from 4 K to 300 K. **C** Variation of the band edge with temperature, as extracted from PL (blue circles) and absorbance (orange diamonds) spectra in **A** and **B** respectively. Variation of the **D** Stokes shift and **E** integrated photoluminescence with temperature from 4 K to 300 K. Vertical dashed lines correspond to key temperatures where we see changes in structural configuration upon heating of the material - 90 K (blue), 220 K (red) and 260 K (black).

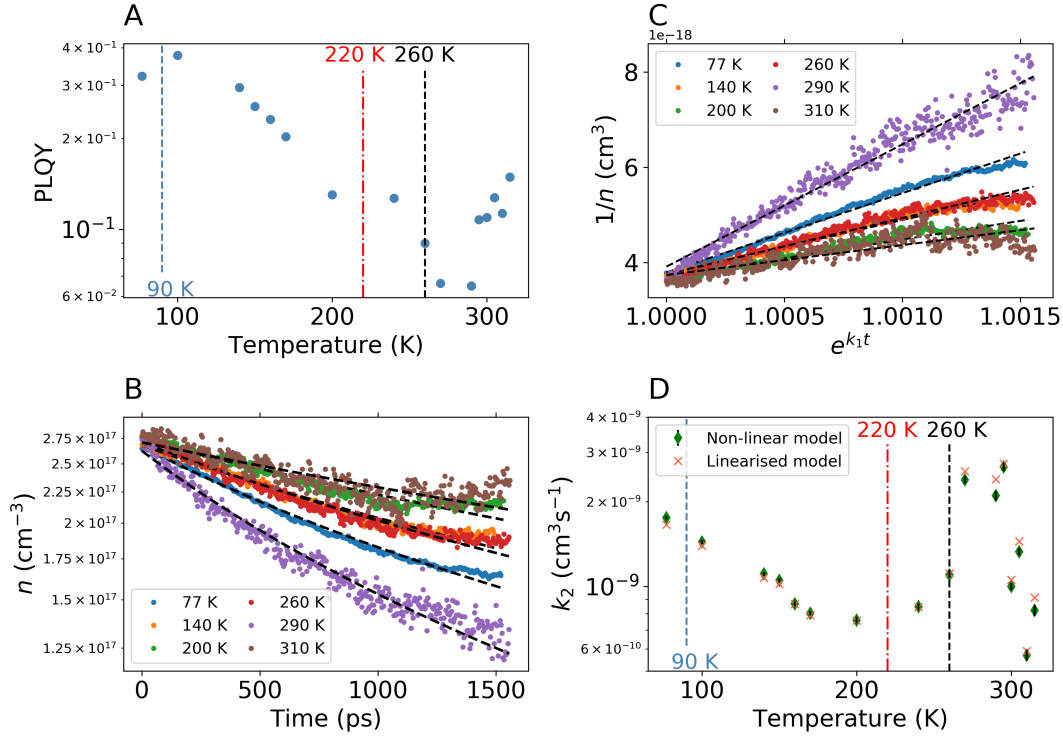


Figure 4: **A** Temperature dependent values of the PLQY, as scaled from the room temperature value using the method shown in the Supporting Information. **B** Charge carrier density n as a function of time as calculated from PL decay traces extracted from streak camera images, taken at a laser fluence of $3.1 \mu\text{Jcm}^{-2}$. Dashed black lines denote fits to the data using the analytical solution to the rate equation, from which temperature-dependent values of k_2 were extracted. **C** Plot of $1/n(t)$ vs $e^{k_1 t}$, which allowed us to linearise the model from Equation (4) and extract values of k_2 by fitting a linear regression to the data. Dashed black lines denote linear fits. **D** Temperature dependence of the bimolecular recombination rate k_2 as determined from fits shown in **B** and **C**. Vertical dashed lines in **A** and **D** correspond to the key temperatures where we see changes in structural configuration upon heating of the material - 90 K (blue), 220 K (red) and 260 K (black).

Table of Contents Entry

The interplay of crystal structure and photophysics in the mixed cation, mixed halide perovskite $(\text{FAPbI}_3)_{0.85}(\text{MAPbBr}_3)_{0.15}$ is probed. It is found that changes in crystal structure, quantified by structural parameters such as lattice constant ratios and bond angles, influence optoelectronic properties in the film - the band gap, Stokes shift and charge carrier recombination rates all exhibit phase specificity.

Keyword: hybrid perovskite solar cells

